

Synthesis of Ag@ZrO₂ nanoparticles: A sensitive electrochemical sensor for determination of antibiotic drug tinidazole

Rajaram Pandiyan^{1,†}, Venkatachalam Vinothkumar^{1,†}, Tse-Wei Chen^{1,2}, Shen-Ming Chen^{1,*}, Manickavasagan Abinaya¹, Syang-Peng Rwei^{2,3}, Heng-Yuan Hsu^{4,5,*}, Chun-Wei Huang^{4,5}, Ming-Chin Yu^{4,5}

¹Department of Chemical Engineering and Biotechnology, College of Engineering, National Taipei University of Technology, No. 1, Section 3, Chung-Hsiao East Road, Taipei 10608, Taiwan, ROC.

²Research and Development Center for Smart Textile Technology, National Taipei University of Technology, No.1, Section 3, Chung-Hsiao East Road, Taipei 10608, Taiwan, ROC.

³Institute of Organic and Polymeric Materials, National Taipei University of Technology, Taiwan.

⁴Department of Surgery, New Taipei Municipal Tucheng Hospital (Built and Operated by Chang Gung Medical Foundation), New Taipei City 23652, Taiwan.

⁵Chang-Gung University, Taoyuan city 33302, Taiwan

[†]Rajaram Pandiyan and Venkatachalam Vinothkumar contributed equally to this work.

*E-mail: smchen78@ms15.hinet.net (shen-ming chen), smallredshoe@gmail.com (Heng-Yuan Hsu)

Received: 18 December 2021 / Accepted: 24 January 2022 / Published: 4 March 2022

The synthesis of metal-doped metal oxides nanostructures has become promising electrode materials to enhance the performance of the electrochemical sensors. This work describes the synthesis of Ag@ZrO₂ nanoparticles through a simplistic co-precipitation route for the electrochemical determination of tinidazole (TNZ). The structural, optical, and morphological properties of Ag@ZrO₂ were characterized with diverse spectroscopic techniques. The electrochemical impedance spectrum (EIS) of the Ag@ZrO₂ electrode displays a higher active surface area of 0.248 cm² than the ZrO₂ electrode (0.172 cm²) and exposes more active sites of Ag@ZrO₂ provides increased electrocatalytic activity for the monitoring of TNZ compared with ZrO₂. The voltammetric methods such as CV and DPV were employed to investigate the electrocatalytic activity of Ag@ZrO₂/GCE. The results indicated that under optimized electrochemical conditions, the fabricated electrode displays an ultra-sensitive detection potential of TNZ at -0.29 V with a wide linear range of 0.2–414.5 μM, and the lowest detection limit (LOD) of 0.073 μM, respectively. The Ag@ZrO₂ sensor demonstrated good stability, precision, and excellent selectivity in various interfering mixtures. The practicability of the Ag@ZrO₂ electrochemical sensor was further confirmed to TNZ in real human serum with acceptable outcomes.

Keywords: Ag@ZrO₂; co-precipitation method; tinidazole; electrochemical sensor; real serum sample.

1. INTRODUCTION

Tinidazole (TNZ, 1-(2-ethyl sulfonyl ethyl)-2-methyl-5-nitroimidazole) is an antibiotic drug that belongs to one of the nitroimidazole derivatives. TNZ is developed to treat vaginal infection trichomoniasis and parasite infections such as amebiasis, and giardiasis [1]. It is also used as an antiprotozoal agent [2]. TNZ has been used to control the growth of microorganisms, especially *Helicobacter pylori*, *Clostridium difficile*, and *Bacteroides* [3]. Further, TNZ can enter into the microorganisms and undergoes a reduction reaction to produce cytotoxic derivatives which directly affect the DNA by irreversible covalent binding. The half-life period of TNZ is 12.3 h and about 63% eliminated being from the human body [4]. The market availability and over usage of TNZ in different formulations initiate the possibility of entering its cytotoxic derivatives into the environment. To determine the leakage during production, heavy dose issues in clinical usage, and over existence in the environment, sensitive and selective determination of TNZ becomes inevitable. Various methods were reported for the qualitative and quantitative determination of TNZ, for instance, spectrophotometry [5], high-pressure liquid chromatography [6], fluorescence quenching [7], spectrofluorimetry [8], liquid chromatography-mass spectroscopy [9], and potentiometry [10] methods. Among these methods, voltammetric detection is a suitable method for TNZ sensing, due to its cost-effectiveness, biocompatibility, environment friendliness, easy operation, and simplicity, which further provides excellent physicochemical characteristics.

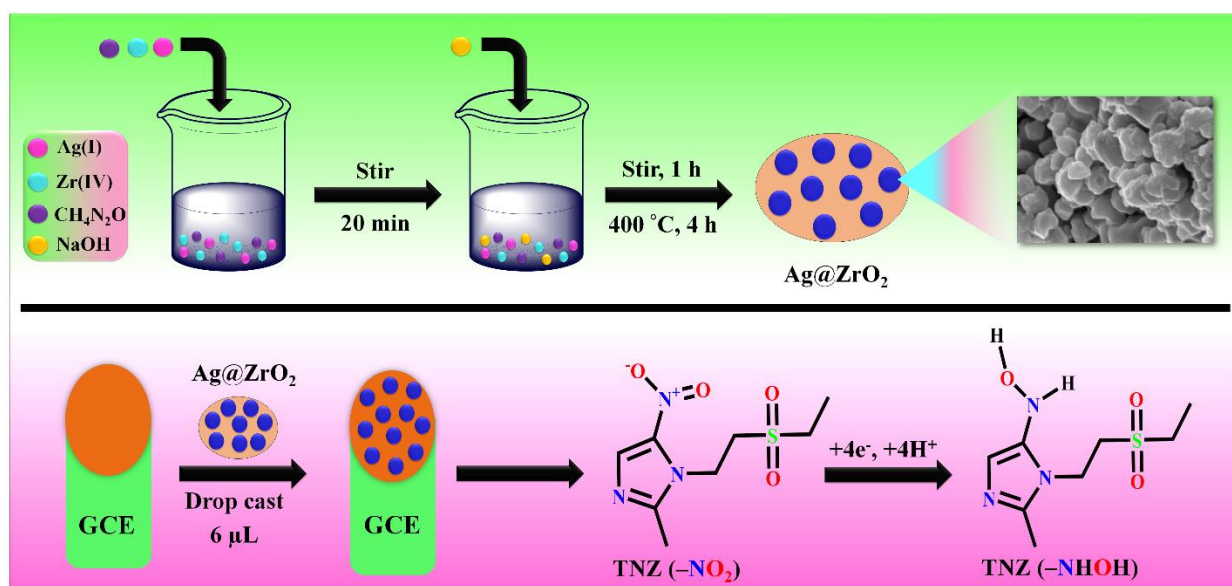
Very few works have been previously reported for the electrochemical detection of antibiotic drug TNZ. For example, A. Taye and M. Amare developed voltammetric determination of TNZ in pharmaceutical tablets using carbon paste electrode (CPE) with results showing a wide linear concentration from 5 to 200 μM [11]. R. Jain et al. constructed polyaniline electrode towards TNZ detection [12]. C. Wang et al. fabricated a poly(carmine) film-modified glassy carbon electrode (GCE) and the electrochemical behavior of TNZ at the modified electrode was investigated [13]. S. Shahrokhian et al. studied the electrochemical monitoring of TNZ on AuNP/CNT modified electrode through LSV analysis with an achieved detection limit is 0.01 μM [1]. Y. Nikodimos et al. prepared a simple electrochemical sensor based on 1,4-BQMCPE that was applied for the TNZ sensing [14]. E. Saeb et al. synthesized Fe-MOF/Pt nanoparticles for the differential pulse voltammetry sensing of TNZ in pharmaceutical tablets and human samples [15]. To bring higher selectivity and sensitivity, various modifiers have been used on these electrode materials.

Metal oxides nanomaterials were widely studied in different applications of electrochemistry such as batteries, supercapacitors, electrocatalytic reactions, photo-electrocatalysis, biosensors, solar cells, sensing devices, energy storage, and conversion [16], because of their unique properties including high conductivity, more catalytic sites, large surface to volume ratio [17][18][19]. Particularly, transition metal oxides were gained much interest due to their tremendous potential in electrode modification and electrochemical applications [16]. Zirconium oxide (ZrO_2) is a p-type semiconducting material that shows exclusive properties with high chemical activity, thermal stability, and non-toxic nature. Due to this distinctive characters of ZrO_2 has been used in various areas for many applications such as nuclear powerplant as they do not absorb neutrons, in the production of hard ceramics and dentistry, as a refractive material in insulators, enamels, abrasives, as a corrosion inhibitor in high-quality pumps and

valves [20]. Zirconia is even used as a protective coating on particles of TiO₂ pigments which displays its superiority over titania in terms of stability [21][22]. Besides, zirconia has three phases namely cubic, tetragonal, and monoclinic, in which only the monoclinic phase is stable at room temperature [23]. Many metal cations were doped into zirconia for stabilizing the most appropriate metastable tetragonal and cubic phases of zirconia at room temperature [24] which exhibits that the doping increases the stability-like properties of zirconia. In this regard, many researchers tried different transition metals dopants (such as Pd, Au, Pt, and Ag) with zirconia for increasing their physicochemical properties. Among all dopants, the metallic silver (Ag) material is an efficient dopant, due to its exclusive characteristics, environmental nature, and low cost than that of other transition metals. Moreover, Ag nanoparticles make high surface energy, which improves surface reactivity (e.g., catalysis) [25]. In addition, Zirconia is an excellent choice with doping of Ag, owing to their remarkable optical, magnetic properties, chemical inertness, metal-support interaction [25], and new catalytic sites thus may favorable for enhancing electrochemical performance in sensor applications.

Over the past decades, ZrO₂ with various dopant-based materials have been synthesized by several methods and applied for different applications. Such as, A. Husain et al. developed a ZrO₂/PTH composite for the detection of ethane gas [26]. L. Zhang et al. studied based on isopolyacid/ZrO₂ combination of fabricating an electrochemical sensor for detecting clenbuterol and ractopamine [27]. S. Zhou et al. prepared ZrO₂/GNF/AuE for the impedimetric determination of osteopontin [28]. S.A. Shahamirifard et al. reported ZrO₂/Au/ChCl as effective material in electrochemical detection of gallic acid and uric acid [29]. N. Gao et al. proposed ZrO₂/Au/Graphene nanocomposite for electrochemical sensing of methyl parathion [30]. H. Mahajan et al. established ZrO₂/rGO nanocomposite and its potential in the electrocatalytic application of anticancer drug [31]. S.A. Alkahtani et al. designed La/ZrO₂/rGO nanosheets as electrocatalyst for the reduction of salinomycin [32]. Recently, S. Vijayalakshmi et al. fabricated ZrO₂/PANI-based electrochemical sensor to decompose the wastewater from drug industries [33]. T. Alizadeh and S. Nayeri examined the electrochemical sensing activity of ZrO₂, and which can be enhanced *via* simple doping of cerium metal nanoparticles for the determination of salicylic acid [34]. P. Bansal et al. introduced gold nanoparticles decorated ZrO₂ for enhancing its electrochemical sensing potential of monitoring hydrazine and catechol [35]. X. Yin et al. boosted solar cells using a flexible and cost-effective counter electrode of Ag@ZrO₂/C nanofiber film, in which the combination of the noble metal with zirconia plays a vital part in the enrichment of the potential [36]. T. Tao et al. developed for voltammetric detection of methyl parathion using Au-ZrO₂ nanocomposite modified graphene electrochemical transistor [37]. L. Li et al. executed a highly sensitive non-enzymatic MP sensor built on electrospun CuO₂ doped ZrO₂ composite microfibers [38]. F. Gonella et al. studied the structural and optical properties of silver-doped zirconia and mixed zirconia-silica matrices have synthesized through the sol-gel technique [39]. E. N. L. Rodrigues et al. studied ZrO₂-based nanoparticles doped with silver using the polymeric precursor method (Pechini), and to validate their bactericidal activity against *Escherichia coli* and *Staphylococcus aureus* [40]. E. Bharathi et al. prepared p-type semiconducting materials of Ag doped ZrO₂ nanoparticles through the hydrothermal method and utilized for photocatalytic degradation of Rh6G dye [41]. T.M.S. Dawoud et al. developed the production of ZrO₂ and Ag doped ZrO₂ nanostructures using milk powder by low-temperature combustion method and has been examined for the degradation of Rhodamine B (RhB) dye in visible light irradiations with

experimental results show good photocatalytic efficacy of 95% [42]. It is worth indicating that the above developed few techniques show complicated preparation methods, operational expensive equipment, and are time-consuming. Usually, the coprecipitation technique is an environmentally friendly, inexpensive, and easy way to synthesize nanomaterials with superior electrochemical enhancement owing to high selectivity and low detection limits. So far, to the best of our research, there are no articles for the determination of TNZ using the cost-effective Ag@ZrO₂ modified electrode. In this study, we synthesized Ag doped ZrO₂ nanoparticles *via* the co-precipitation approach towards the electrochemical analysis of TNZ. The as-prepared Ag@ZrO₂ were examined with various spectrometric studies. The Ag@ZrO₂ modified electrode revealed an excellent sensing activity of TNZ detection than the bare electrode. The electrochemical reduction of TNZ was succeeded by a WLR, low LOD, high selectivity, reproducibility, good stability, and repeatability at the modified sensor. Finally, the as-fabricated Ag@ZrO₂/GCE was used for TNZ monitoring in human serum with noticeable recoveries.



Scheme 1. The schematic illustration of as-prepared Ag@ZrO₂ nanoparticles for the sensitive voltammetric sensing of TNZ.

2. EXPERIMENTAL SECTION

2.1 Chemicals

Silver nitrate (AgNO₃, 99.99%), zirconyl chloride octahydrate (ZrOCl₂·8H₂O, 98%), urea (CH₄N₂O, 99%), ethylene glycol (C₂H₆O₂, 99.8%), sodium hydroxide (NaOH, ≥97.0%), tinidazole (C₈H₁₃N₃O₄S, 99.6%), monosodium phosphate (NaH₂PO₄, 98%), and disodium phosphate (Na₂HPO₄, 99%) were purchased from Sigma-Aldrich. For electrochemical investigations, distilled water was used throughout the work for the preparation of all aqueous solutions. The prepared (0.05 M phosphate buffer

(PB) solution) pH values such as 3.0, 5.0, 7.0, 9.0, and 11.0 were adjusted by using 0.1 M HCl and NaOH.

2.2 Synthesis of Ag@ZrO₂ nanoparticles

The synthesis of Ag@ZrO₂ nanoparticles was followed by our previous report based on slight variations [43]. 0.1 M of AgNO₃ and 0.2 M of ZrOCl₂·8H₂O, 0.3 M of CH₄N₂O were dissolved in 100 mL of distilled water were vigorously mixed for 20 min under a magnetic stirrer. After that, 2 M of NaOH (10 mL) was added drop by drop above the mixture with continuous stirring (600 rpm) for 1 h at room temperature. The obtained precipitate was cooled down naturally and washed with H₂O/C₂H₅OH. The resultant precipitate was dried at 50 °C for 12 h. The dried precipitate was calcinated at 400 °C for 4 h at a heating rate of 5 °C min⁻¹, respectively. The collected precipitate was designated as Ag@ZrO₂ nanoparticles are demonstrated in Scheme 1. For the electrochemical comparison study, ZrO₂ has been prepared by the same experimental conditions without the addition of the silver precursor.

2.3 Techniques

The phase structure and crystallinity of as-synthesized Ag@ZrO₂ were examined by X-ray diffraction (XRD) using Malvern PANalytical, the Netherlands in Cu K α (1.5406 Å) radiation. Fourier transform infrared spectra (FT-IR) were determined in the range of 4000–400 cm⁻¹ using a JASCO 4600LE Shimadzu spectrometer in Japan. The absorption bands were studied using a UV-diffractive reflectance spectrophotometer (JASCO V-770 from Japan). The optical properties were analyzed by photoluminescence (PL) spectrometer using Ramboss-500i, Dongwoo Optron Co., Ltd., Korea. UniNanoTach, ACRON (South Korea) was used to study the Raman spectrum. The morphological and surface properties were performed in the FESEM (JEOL-JSM-6500F) along with energy dispersive X-ray (EDX), and mapping studies. X-ray photoelectron microscopy (XPS) with a Thermo scientific multi-lab 2000 in the United States demonstrated the presence of Ag, Zr, and O molecules in Ag@ZrO₂. The electrocatalytic performance of the Ag@ZrO₂ electrode was investigated through cyclic voltammetry (CV, CHI 1205B), electrochemical impedance spectroscopy (EIS; XPot–ZAHNER–Elektrik instrument), and differential pulse voltammetry (DPV, CHI 410A) techniques. The electrochemical CH instrument with the cell setup has the three-electrode system whereas, the glassy carbon electrode (GCE) as a working electrode, Ag/AgCl, and platinum wire (Pt) was acted as reference and counter electrodes, respectively.

2.4 Fabrication of Ag@ZrO₂/GCE

For the electrode fabrication, the glassy carbon electrode was well polished using 0.05 μ m of alumina slurry. Then, 5.0 mg of Ag@ZrO₂ material was dispersed in 1.0 mL of H₂O and ultrasonication for 30 min. Subsequently, 6.0 μ L of the prepared Ag@ZrO₂ catalyst was drop cast in the well-cleared

GCE and dried in an oven at 50 °C for perfect fabrication of Ag@ZrO₂/GCE. All the voltammetric experiments were conducted using 0.5 M PB for the sensing of TNZ at 0 to -0.9 V.

3. RESULTS AND DISCUSSION

3.1. Structural characterizations of Ag@ZrO₂

The crystalline structure of Ag@ZrO₂ material was characterized by XRD analysis is revealed in Fig. 1a. The characteristic diffraction peaks at $2\theta = 17.54, 24.09, 24.50, 28.21, 31.47, 34.19, 35.30, 40.79, 41.18, 44.83, 45.54, 49.32, 50.16, 50.61, 51.25, 54.12, 55.47, 55.95, 57.20, 57.91, 58.31, 59.94, 62.02, 65.70, 71.27, \text{ and } 75.23^\circ$ were corresponding to the planes of (100), (011), (110), (111), (-111), (002), (200), (211), (-102), (-112), (202), (022), (220), (122), (221), (-202), (013), (130), (-310), (131), (222), (-131), (213), (-222), (104), and (041), respectively. All the diffraction peaks were well-matched in the monoclinic structure of ZrO₂ (JCPDS. 00-007-0343) [44]. Besides, the presence of five diffraction peaks at $2\theta = 38.20, 44.40, 64.60, 77.60, \text{ and } 81.75^\circ$, which is assigned to the (111), (200), (220), (311), (222) planes of face-centric cubic structured Ag metal nanoparticles standard peaks were confirmed in the JCPDS. 01-087-0720 pattern [45], these results suggest that the Ag has efficaciously doped into ZrO₂ without impurities or other phases. The average crystalline size (D) was further examined according to Scherer's formula (1) [31][35],

$$D = \frac{K\lambda}{\beta \cos \theta} \quad (1)$$

Here $k, \lambda, \theta,$ and β represents the Scherer constant (0.68), the wavelength of X-rays (1.5406 Å), the diffraction angle of the high-intensity peaks, and the full width at half maximum (FWHM) of the diffraction peak, respectively. Given to equation (1), the calculated Ag@ZrO₂ average crystalline size is ~20.218 nm at the dealing temperature of 400 °C. These results approve that the formation of Ag@ZrO₂ with high purity and crystallinity.

The FT-IR spectrum of Ag@ZrO₂ in the range from 4000–400 cm⁻¹ is presented in Fig. 1b. The FT-IR bands at 526 and 747 cm⁻¹ were ascribed to the stretching vibration modes of Zr–O, and Ag–O [46][47]. It is clear that there must be an attachment between silver and zirconium *via* oxygen, which could be the manifestation of doping. Fig. 1c shows the UV-DRS spectrum of Ag@ZrO₂ in the range between 200 to 800 nm. The absorbance peak at 277 nm exactly belonged to zirconia because a lower wavelength occurred in the valence to conduction band transition [48]. However, the absorption of doped material produced at 312 nm corresponds to M–O bond is assigned for Zr–O and not for dopant ions [49]. The peak at 335 nm is attributed to the silver nanoparticles due to the blue shift oxygen interference from zirconia. Doping of silver increased the surface defects and the surface to volume ratio in the Ag@ZrO₂, thus there could be more available active sites [50]. The peaks obtained at about 212 and 255 nm were agreeing to the typical vibrations of the monoclinic zirconia [51][52].

The photoluminescence spectrum of Ag@ZrO₂ nanoparticles prepared at 400°C are illustrated in Fig. 1d. It has a blue emission at ~488 nm is ascribed to the rich flaws such as dislocation, which are beneficial for quick oxygen movement [53][54]. Furthermore, Raman analysis was employed by the

functional bands of as-synthesized Ag@ZrO₂ is depicted in Fig. 1e. The obtained Raman active peaks were compared with previous reports of zirconia in three phases. The peaks at 86, 181, 339 cm⁻¹ are agreeing with the monoclinic phase of zirconia and the broad peak at 630 cm⁻¹ was attributed to monoclinic as well as slightly cubic phase structures in Ag@ZrO₂ [55][56]. The additional Raman peak at 482 nm was attributed to Ag–O bond [50].

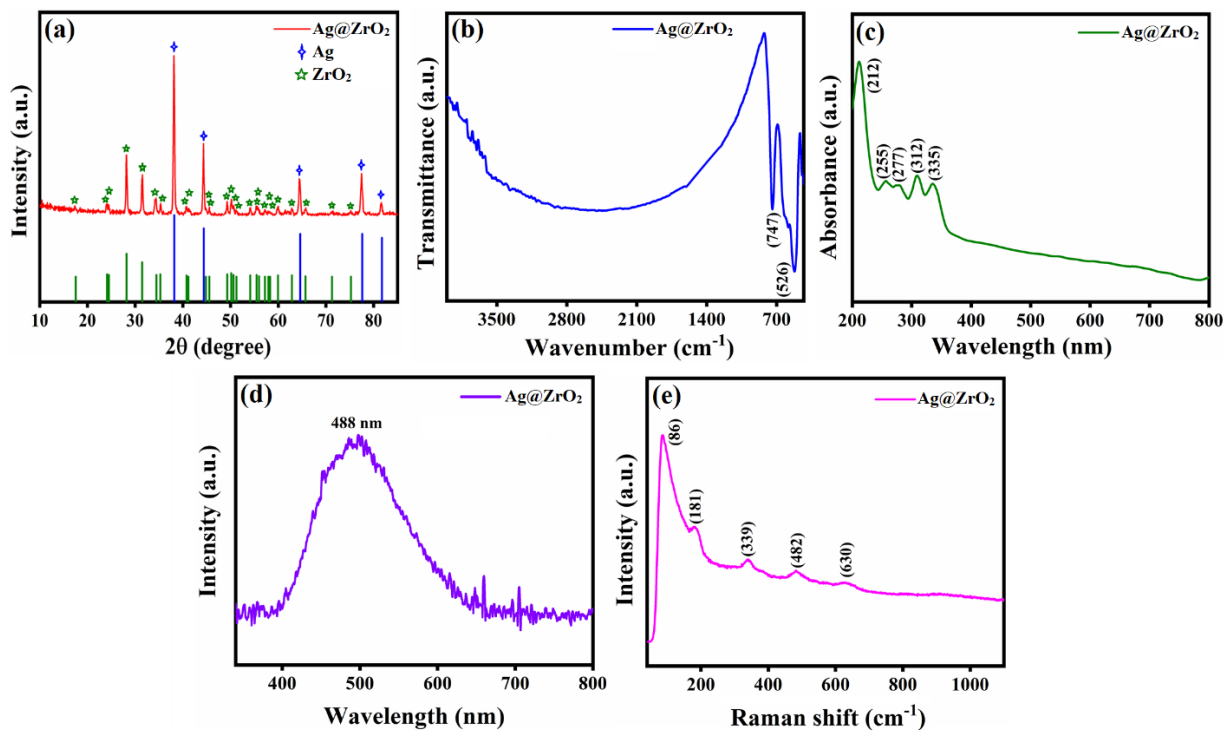


Figure 1. (a) XRD, (b) FTIR, (c) UV-DRS, (d) PL, and (e) Raman spectrum of Ag@ZrO₂.

The structural morphology of Ag@ZrO₂ was evaluated using FESEM analysis, as displayed in Fig. 2a–c. The FESEM micrograph of Ag@ZrO₂ nanoparticles reveals smaller pebble-like shapes that turn into big stony structures.

The intermolecular interaction between the produced nanoparticles causes agglomeration. These images also reveal the size of the nanostructures has less than ± 100 nm. Moreover, the mixed elemental mapping image (Fig. 2d) of Ag@ZrO₂ exhibits that the elements were evenly spread over throughout the nanostructures (see Fig. 2e–g). As displayed in (Fig. 2h) EDX spectrum of Ag@ZrO₂, the presence of elements such as Ag, Zr, and O in the Ag@ZrO₂ was confirmed and the composition of the elements was found to be 29.3% (Ag), 54.0% (Zr), and 16.7% (O), respectively. This confirms the effective formation and doping of Ag into Ag@ZrO₂.

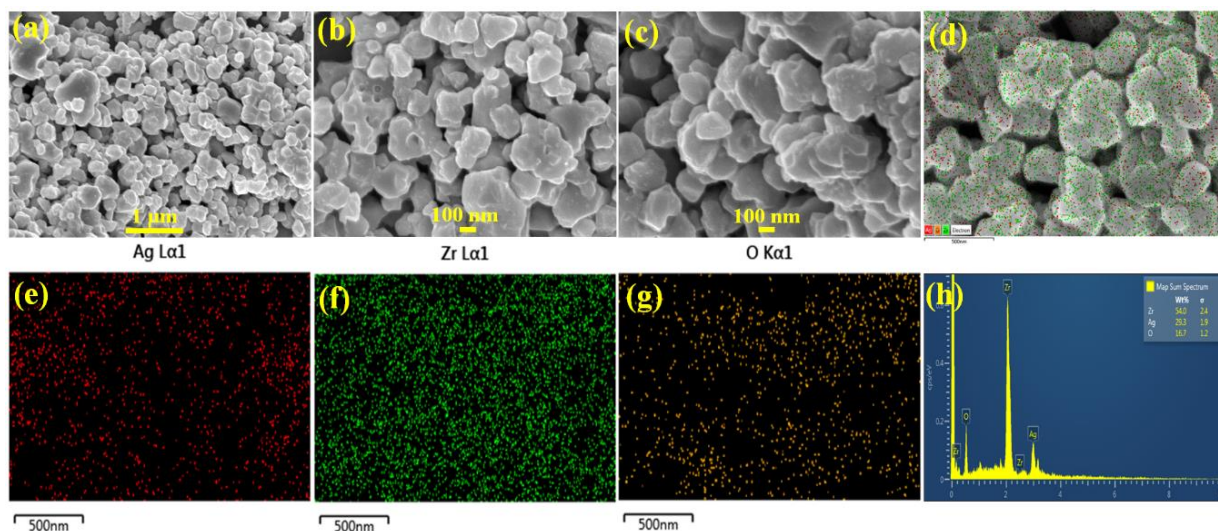


Figure 2. (a–c) FE-SEM images of the Ag@ZrO₂, (d) elemental mapping mixture of Ag@ZrO₂, and the matching each element of (e) Ag, (f) Zr, and (g) O, and (h) EDX spectrum with elemental weight percentage.

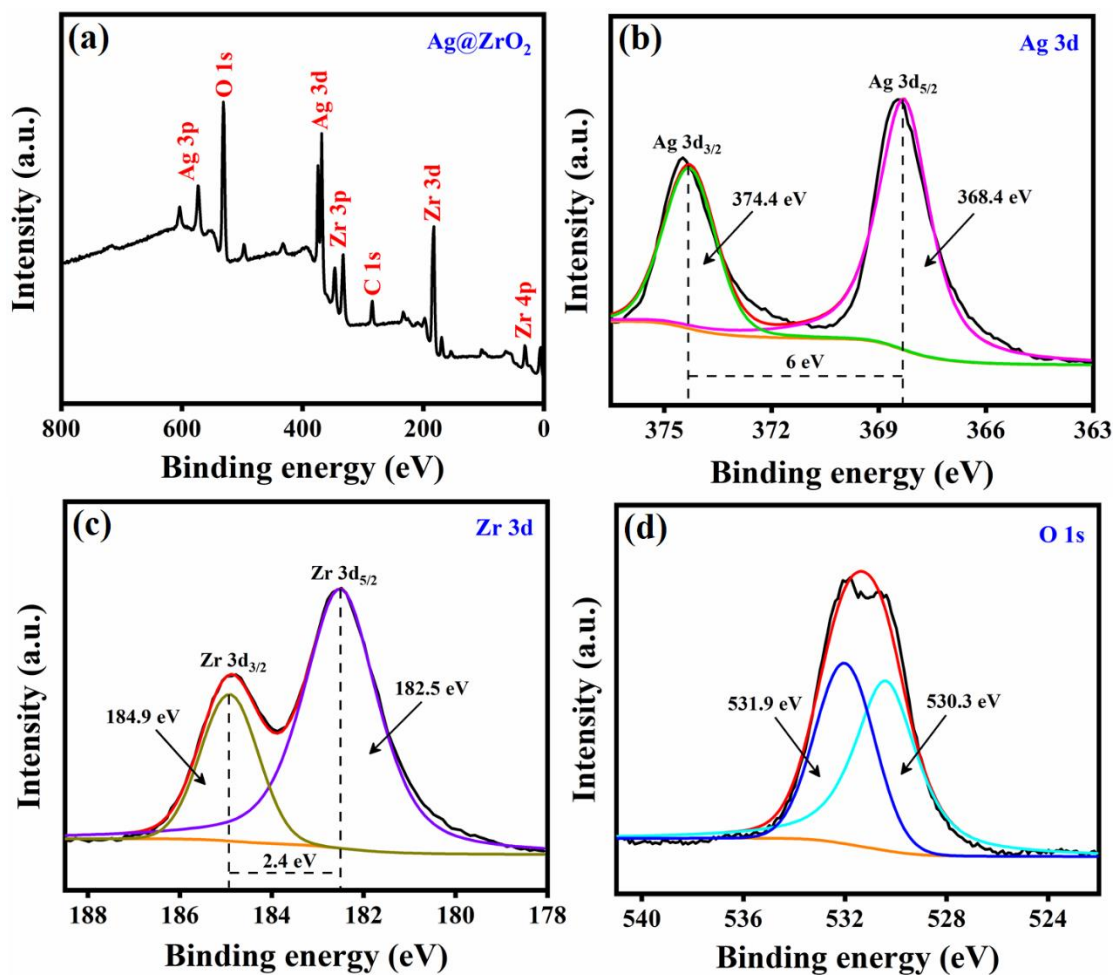


Figure 3. (a) XPS full survey scan, (b) Ag 3d, (c) Zr 3d, and (d) O 1s in the Ag@ZrO₂.

X-ray photoelectron spectroscopy analysis of as-synthesized Ag@ZrO₂ was carried out to study the chemical composition and atomic states of the elements are demonstrated in Fig. 3. The survey spectrum (Fig. 3a) reveals the presence of the Ag, Zr, and O elements in Ag@ZrO₂. The enlarged high-resolution spectra of Ag 3d, Zr 3d, and O 1s were given in Fig. 3b–d, respectively. The binding energy peaks at 368.4 and 374.4 eV corresponds to Ag 3d_{5/2} and 3d_{3/2} spin states (Fig. 3b). The peak variations of Ag 3d_{5/2} and Ag 3d_{3/2} were calculated at about 6.0 eV is in good agreement with the previously reported value [57]. This result strongly supports the construction of metallic Ag. The binding energies at around 182.5 and 184.9 eV were attributed to the zirconium of 3d_{5/2} and 3d_{3/2} [36] is shown in Fig. 3c. The spin-orbit splitting of the two peaks (Zr 3d_{5/2} and Zr 3d_{3/2}) is 2.4 eV, confirming the presence of the Zr⁴⁺ oxidation state of the as-prepared sample. The element of O1s (Fig. 3d) displays two different binding energies at 530.3 and 531.9 eV relates to Zr–O and O–H bonding [58]. Above the analytical systems namely XRD, FT-IR, Raman, UV-DRS, PL, FESEM, and XPS results prove that the as-proposed Ag is well doped in ZrO₂ to the build of Ag@ZrO₂. Additionally, the C 1s peak shows the absorption of water molecules from the atmospheric moisture.

3.2 Electrochemical behavior of Ag@ZrO₂/GCE

The electron transfer resistance (R_{ct}) of the proposed electrodes of bare GCE, ZrO₂/GCE, and Ag@ZrO₂/GCE was investigated by using an EIS experiment in 0.1 M KCl/5 mM [Fe(CN)₆]³⁻ and 5 mM [Fe(CN)₆]⁴⁻ solution at the potential frequency of 0.1 Hz→100 kHz with the detected potential of 10 mV. Fig. 4a inset shows the Randles circuit dependent on two frequencies: (1) the semicircle diameter of the high-frequency region is assigned to R_{ct} , and (2) the low-frequency linear region is corresponding to diffusion rate kinetics. The observed R_{ct} value of bare GCE was evaluated to be 92 Ω , due to the Ferri/Ferrocyanide system's reversible redox activity and GCE [59]. The modified ZrO₂/GCE shows a larger resistance value of 1398 Ω , which is a poor electron transfer rate than the bare electrode. After the doping of Ag in ZrO₂/GCE was estimated at the lower impedance of 746 Ω owing to the high electroconductivity and fast electron transfer efficiency of Ag@ZrO₂.

The obtained CVs of bare GCE, ZrO₂/GCE, and Ag@ZrO₂/GCE in the presence of 0.1 M KCl and 5 mM [Fe(CN)₆]^{3-/4-} solution at the scan rate of 50 mV s⁻¹ as portrayed in Fig. 4b. From these CVs, the bare electrode demonstrates a well-defined redox peak current, indicating the dirt and oxide layer on the GCE's surface was cleaned and polished, according to this result [60]. The lower oxidation and reduction peak current occurred in ZrO₂/GCE ($I_{pa} = 52.51 \mu\text{A}$, and $I_{pc} = -50.48 \mu\text{A}$) with the larger peak-to-peak separation (ΔE_p) of 0.23 V, respectively. The modified Ag@ZrO₂/GCE shows the highest redox peak current ($I_{pa} = 62.85 \mu\text{A}$, and $I_{pc} = -62.96 \mu\text{A}$) and lowest peak separation ($\Delta E_p = 0.17 \text{V}$), suggesting the modified electrode has a good electron transfer pathway in the redox couple reaction (Fe²⁺/Fe³⁺). These results were consistent with EIS analysis. Additionally, the anodic/cathodic current (I_{pa}/I_{pc}) increases while increasing the scan rates from 20 to 200 mV s⁻¹ in Fig. 4c. The linear plot (Fig. 4d) between redox peak current and the square root of the scan rate ($v^{1/2}$) evidences the modified sensor is a diffusion-controlled electrochemical process. Furthermore, the electroactive surface area (A) was calculated in the following Randles–Sevcik equation (2) [61],

$$I_p = 2.69 \times 10^5 A D^{1/2} n^{3/2} v^{1/2} C \quad (2)$$

Here I_p , A , D , n , v , and C represent the redox peak current, active surface area, diffusion coefficient, total number of transfer electrons, scan rate, and addition of a 5 mM Ferri/Ferrocyanide system. From equation (2), the A was estimated as 0.172 and 0.248 cm² for ZrO₂/GCE, and Ag@ZrO₂/GCE, respectively. It suggests that the Ag@ZrO₂/GCE improves the active surface area and promotes the response of electrochemical signals in the target detection.

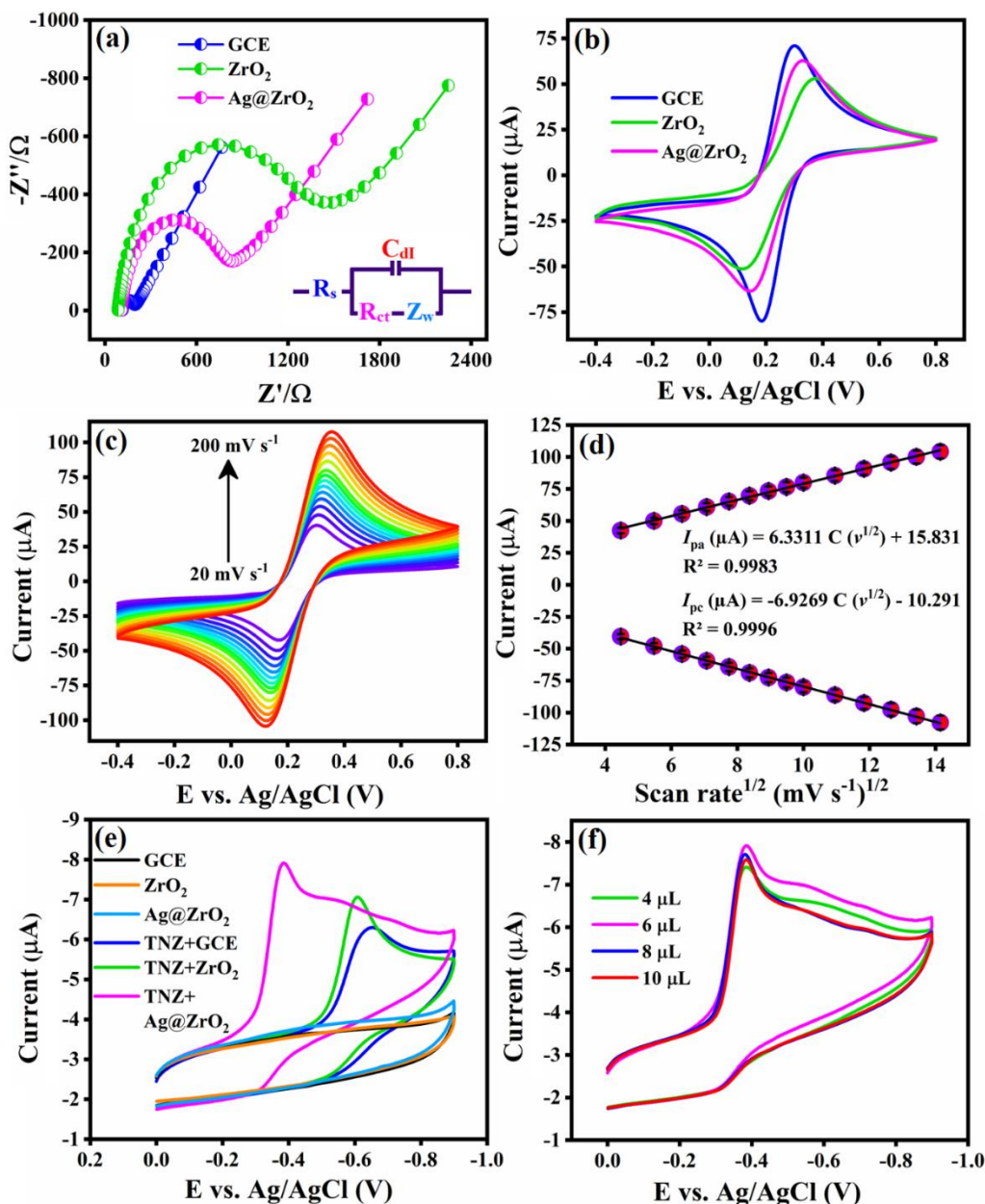


Figure 4. (a) EIS, and (b) CV of bare GCE, ZrO₂/GCE and Ag@ZrO₂/GCE in 0.1 M KCl/5 mM [Fe(CN)₆]^{3-/4-} solution, (c) CV response of Ag@ZrO₂ modified GCE with diverse scan sweeps (20–200 mV s⁻¹), (d) the plot of I_{pa}/I_{pc} vs $v^{1/2}$, (e) CV for bare GCE, ZrO₂/GCE, and Ag@ZrO₂/GCE in the absence and presence of 75 μM TNZ in pH 7.0 (0.05 M PB) at 50 mV s⁻¹ scan rate, and (f) CV curves of the I_{pc} peak current on Ag@ZrO₂ sensor with different loading concentration of TNZ (75 μM).

3.3 Electrocatalytic performance of TNZ on Ag@ZrO₂/GCE

The electroreduction activity was studied by CV in the absence and presence of TNZ on bare GCE, ZrO₂/GCE, and Ag@ZrO₂/GCE in 0.05 M phosphate buffer (pH 7.0) at the scan rate of 50 mV s⁻¹. As presented in Fig. 4e, there is no peak appeared in the absence of bare GCE, ZrO₂/GCE, and Ag@ZrO₂/GCE. Meanwhile, the background current response of the Ag@ZrO₂/GCE is higher than the other electrodes, demonstrating the Ag@ZrO₂ modified GCE has a good surface area and enhanced conductivity. The resultant CV current response in the presence of 75 μM TNZ, the bare GCE appearances lower reduction peak current at $I_{pc} = -6.28 \mu\text{A}$ with the overpotential of -0.65 V . After the modification of ZrO₂/GCE, the reduction peak potential (E_{pc}) slightly shifted to a positive direction (-0.60 V) and increased reduction current observed at about $I_{pc} = -7.04 \mu\text{A}$ compare to bare GCE, indicating the ZrO₂ could be adsorbed on the surface of TNZ resulting enhance sensitivity. In contrast, Ag@ZrO₂ modified electrode exhibits a much lower reduction peak potential of -0.38 V with a higher reduction peak current noted at $I_{pc} = -7.91 \mu\text{A}$ than that of others with the same amount of TNZ. Besides, the reduction peak potential of TNZ on Ag@ZrO₂/GCE was shifted to the overpotential of -0.22 V and -0.27 V compared with ZrO₂/GCE and bare GCE, respectively, which can facilitate a large number of active sites to support the affinity and activation of the Ag@ZrO₂/GCE towards TNZ with the four-electron transmission [13]. Further, no oxidation peak was detected from the reverse scan, suggesting that the overall reaction of TNZ is an irreversible process for the electrodes of Ag@ZrO₂/GCE, ZrO₂/GCE, and bare GCE.

From the optimal voltammetric conditions, the effect of loading catalyst was performed on Ag@ZrO₂/GCE with different volumes (4.0, 6.0, 8.0, and 10.0 μL) at an applied scan sweep of 50 mV/s using 0.05 M PB (pH 7.0) solution in the presence of 75 μM TNZ is given in Fig. 4f. The observed I_{pc} current increased gradually with an increasing volume of 4–6 μL. Then, the I_{pc} current progressively decreased with an increase in the volume of 8–10 μL attributed to a poor catalytic response due to the bonding adhesion on the electrode surface. Hence, 6.0 μL of Ag@ZrO₂/GCE was succeeded maximum reduction current ($I_{pc} = -7.91 \mu\text{A}$) than other volumes of 4.0 μL, 8.0 μL, and 10.0 μL were measured as $I_{pc} = -7.38 \mu\text{A}$, $-7.57 \mu\text{A}$, and $-7.70 \mu\text{A}$, respectively. It is shown that the highest catalytic activity of 6.0 μL of Ag@ZrO₂/GCE was used for further electroreduction analysis of TNZ.

3.4 Influence of pH towards TNZ

The CV studies were carried out by Ag@ZrO₂ modified GCE in the diverse pHs from 3.0 to 11.0 at the scan rate of 50 mV s⁻¹ with the concentration of 75 μM TNZ in 0.05 M PB. Fig. 5a displays that the I_{pc} current increases with an increase in pH of 3.0 to 7.0. After, I_{pc} current decreases with a rise in the pH above 7.0, suggesting the proton involves in the irreversible reduction process of TNZ. Therefore, the highest reduction current has been achieved at pH 7.0 for TNZ detection, which is well suitable for further electrochemical examinations. Fig. 5b exhibits the plot of different pHs vs reduction current and peak potential with correlation coefficient were follows $I_{pc} (\mu\text{A}) = -0.011 \text{ C (pH)} - 0.3148$ ($R^2 = 0.9908$). In addition, the possible electrocatalytic reduction mechanism of TNZ, the nitro group ($-\text{NO}_2$) directly

involves four-electrons (e^-) and four protons (H^+) transfer to the derivative of hydroxylamine species ($-NHOH$) [13][14], as presented in Fig. 5c.

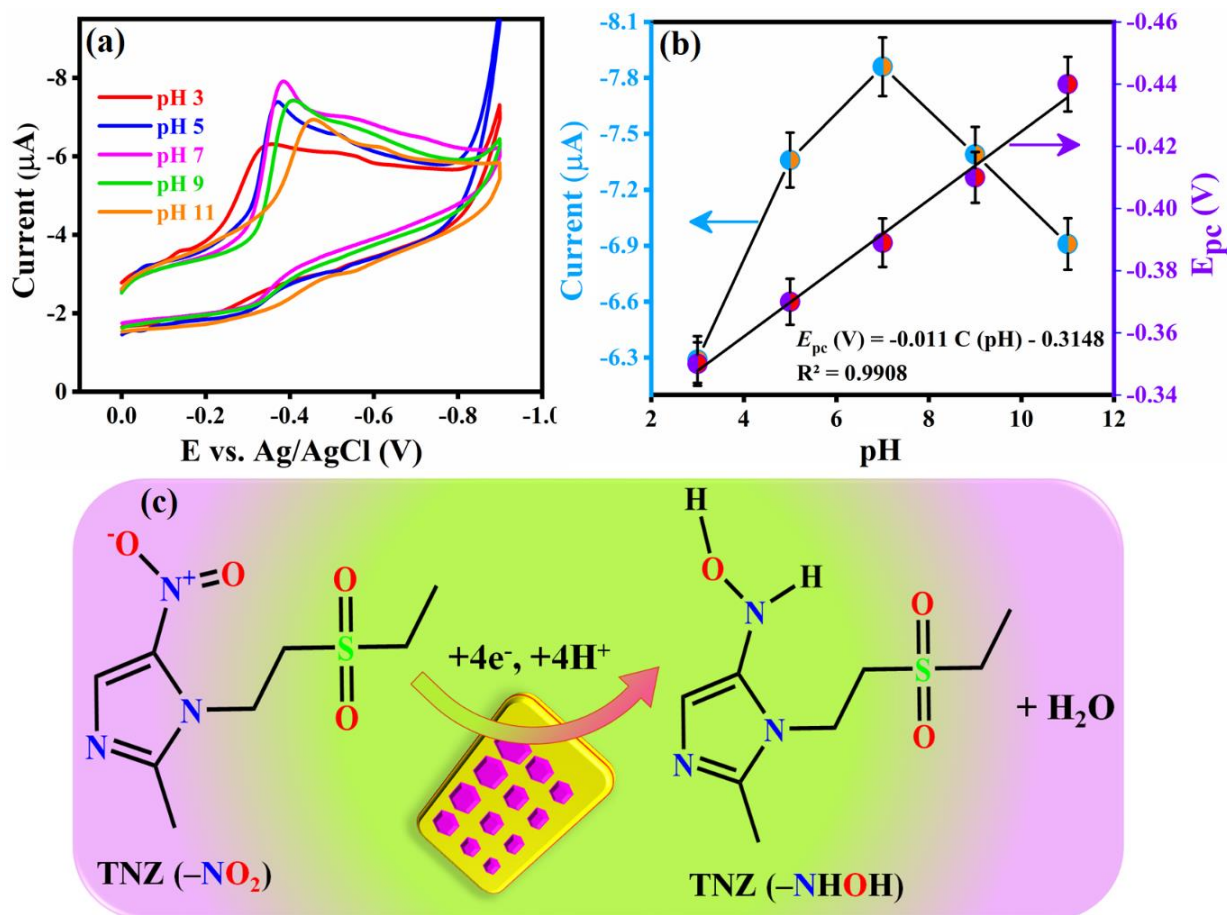


Figure 5. (a) CV curves of Ag@ZrO₂/GCE with diverse pHs 3.0, 5.0, 7.0, 9.0, and 11.0 in 0.05 M PB solution at 50 mV s⁻¹ towards 75 μM TNZ, (b) the plot shows I_{pc} and E_{pc} vs pHs (3.0–11.0), and (c) the probable electroreduction mechanism of TNZ at the Ag@ZrO₂/GCE.

3.5 Influence of concentration on TNZ

Fig. 6a establishes CV curves of Ag@ZrO₂/GCE in pH 7.0 (0.05 M PB) at 50 mV/s scan rate with various enhancing addition of TNZ from 0–200 μM. The noted peak current (I_{pc}) steadily enlarged by increasing the TNZ concentration (0–200 μM). The linear diagram (Fig. 6b) between peak current (I_{pc}) and addition of TNZ (μM) with correlation coefficient was calculated by $I_{pc} (\mu A) = 0.0551 C [\mu M] - 4.0754$ ($R^2 = 0.9985$). These results exhibit that the obtained sharp peak has excellent sensing ability for the detection of TNZ using Ag@ZrO₂/GCE.

3.6 Influence of scan rate for TNZ

The effect of the scan rate is directly related to the electron transfer kinetics between the surface electrode and electrolyte solution. CV was examined by Ag@ZrO₂/GCE with different scan rates (20–200 mV s⁻¹) in 50 μM TNZ using 0.05 M PB (pH 7.0) as depicted in Fig. 6c.

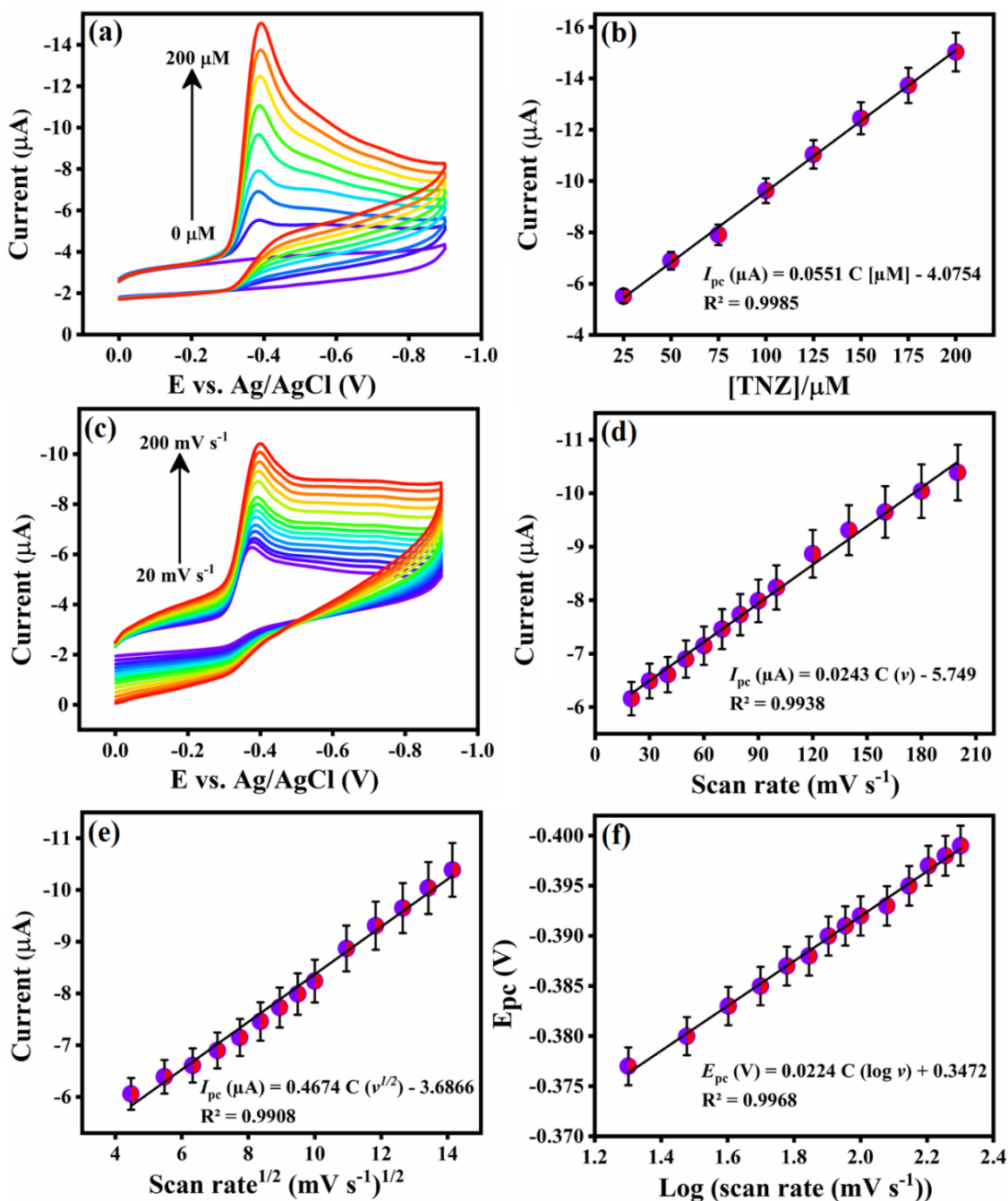


Figure 6. (a) CV response of Ag@ZrO₂ modified GCE with varying concentration of TNZ (0–200 μM), (b) the linearity of I_{pc} vs concentration of TNZ, (c) CV of 50 μM TNZ at Ag@ZrO₂ electrode with changing diverse scan rates (up to 200 mV s⁻¹), (d) the calibration curve I_{pc} current vs ν , (e) linear graph showed I_{pc} current vs $\nu^{1/2}$, and (f) the linear plot between peak potential (E_{pc}) and logarithmic of scan rate ($\log \nu$). The obtained results were used in nitrogen saturated 0.05 M phosphate buffer (pH 7.0).

The CV curves indicate the reduction peak current increased progressively with increasing scan sweeps from 20–200 mV s⁻¹. The plot (see Fig. 6d) of reduction peak current (I_{pc}) versus scan rate (v) with their linear equation were found as I_{pc} (μA) = 0.0243 C (v) – 5.749 ($R^2 = 0.9938$), showing the electrochemical behavior of TNZ at the Ag@ZrO₂/GCE obeys adsorption controlled kinetics. Moreover, the reduction peak current versus square root of scan rate exhibits a linear equation of I_{pc} (μA) = 0.4674 C ($v^{1/2}$) – 3.6866 ($R^2 = 0.9908$), as exposed in Fig. 6e, indicates that the reduction of TNZ is also obeying diffusion-controlled kinetics. These results clarify that the overall electroreduction of TNZ on Ag@ZrO₂ modified GCE is a mixed controlled kinetic process [62][63][64]. Further, the plot (Fig. 6f) amongst the reduction peak potential (E_{pc}) and logarithmic of scan rate ($\log v$) exhibits a regression equation: E_{pc} (V) = 0.0224 C ($\log v$) + 0.3472 ($R^2 = 0.9968$), respectively. According to the Laviron theory, the electron transfer number (n) was calculated by E_p equation (3) [65],

$$E_p = E^0 + \frac{2.303 RT}{\alpha n F} \log \frac{RT k^0}{\alpha n F} + \frac{2.303 RT}{\alpha n F} \log v \quad (3)$$

Here E^0 = formal potential, α = electron transfer coefficient, n = the electron transfer number, k^0 = heterogeneous rate constant and v = scan rate, respectively. Given slope value is 0.0224, $F = 96480$ C/mol, $R = 8.314$ J/K mol, and $T = 293$ K, respectively. The calculated αn value is 2.59 and the found α value is 0.55, which is the complete irreversible electrode [66][67]. Applying equation (3), the electron transfer number was estimated to be ~4.71 (considering to 4), which is in agreement with earlier reported works [11][14], indicating the modified electrode is four electrons ($4 e^-$) and four protons ($4 H^+$) transfer for the reduction of TNZ with the irreversible process.

3.7 Determination of TNZ on Ag@ZrO₂/GCE by DPV method

DPV method exhibits a wide linear range (WLR), high selectivity, low detection limit (LOD), and quantification limit (LOQ) than other voltammetric methods. Fig. 7a displays DPV curves of Ag@ZrO₂/GCE with diverse TNZ concentration in 0.05 M PB (pH 7.0) solution with potential window of 0 to –0.9 V and their parameters were used as follows: sensitivity = 10⁻⁴, modulation time = 2 s, interval time = 0.2 s, step potential = 0.004 V, and pulse amplitude = 0.05 V, respectively. The I_{pc} current increases considerably while increasing TNZ concentrations of 0.2 μM to 414.5 μM with E_{pc} potential were obtained at about $E_{pc} = -0.29$ V (versus Ag/AgCl). The linearity plot (Fig. 7b) shows the relation of I_{pc} current vs concentration of TNZ (0.2–414.5 μM), the regression equation was followed by I_{pc} (μA) = 0.0488 C [μM] – 1.5266 ($R^2 = 0.9958$). The calculated LOD and LOQ is applied *via* using equations (4,5) [63][67],

$$LOD = \frac{3\sigma}{q} \quad (4)$$

$$LOQ = \frac{10\sigma}{q} \quad (5)$$

Here σ is three blank measurements value (0.012) of the standard deviation, and q is the linear plot of the slope value. Substituting equations (4,5), the found LOD and LOQ are 0.073 and 0.246 μM with a sensitivity of 0.669 $\mu\text{M}^{-1} \text{cm}^{-2}$. These voltammetric results reveal that the proposed Ag@ZrO₂/GCE has enhanced electrocatalytic performance for the detection of TNZ than the earlier

reported materials. Besides, Table 1 results concluded that the Ag@ZrO₂/GCE is a good sensing platform for the testing of TNZ.

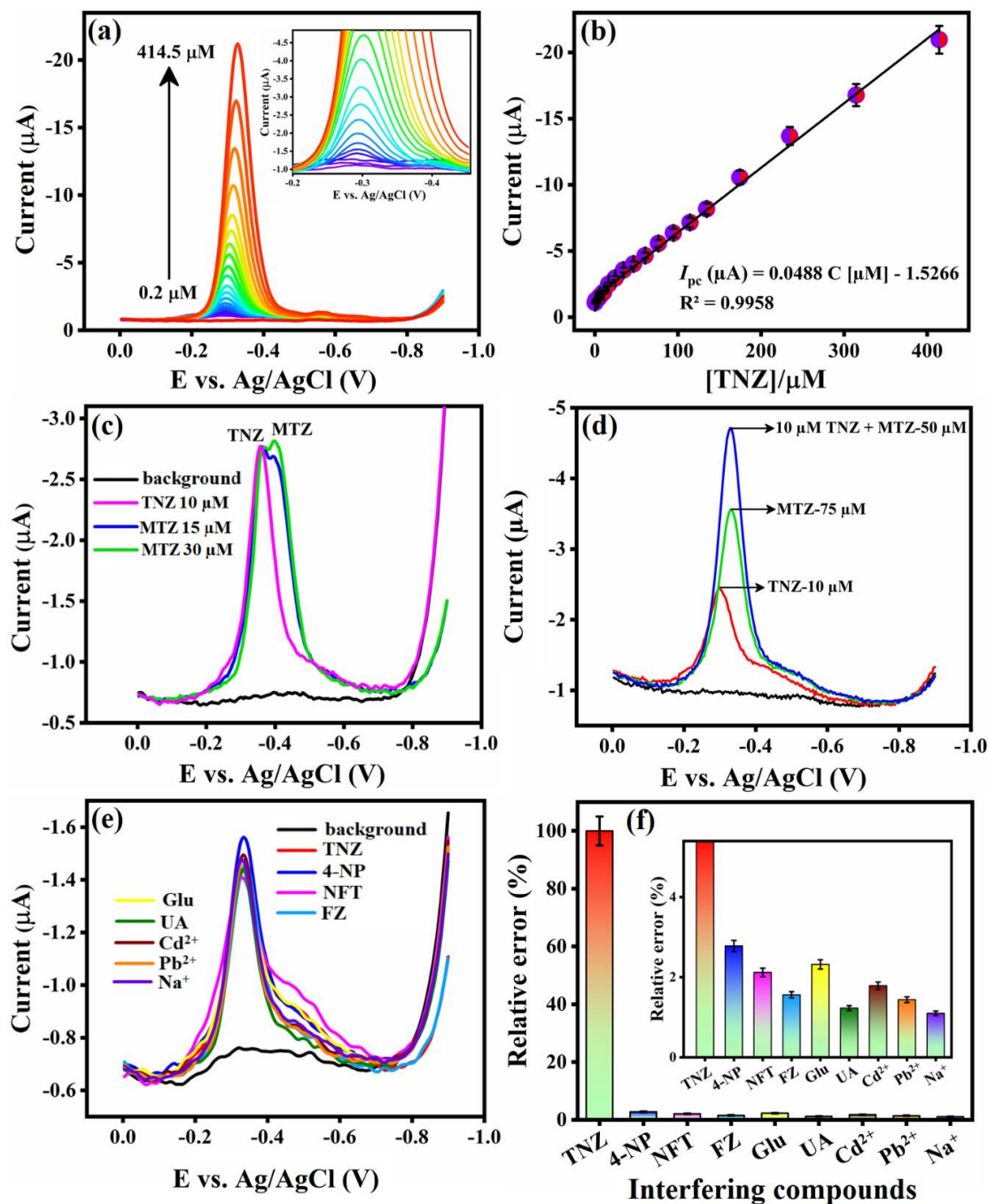


Figure 7. (a) DPV current response of Ag@ZrO₂ modified GCE with increasing concentration of TNZ from 0.2–414.5 μM, (b) the plot between reduction peak current and concentration of TNZ, (c,d) DPV shows the lower and higher amount detection of TNZ and MTZ molecules, (e) DPV studies on modified electrode displays possible interfering molecules such as 4-NP, NFT, FZ, Glu, UA, Cd²⁺, Pb²⁺, and Na⁺ to the detection of 5 μM TNZ in 0.05 M PB, and (f) the bar diagram of relative error *versus* interfering species. The results were used the DPV technique in 0.05 M PB solution (pH 7.0) at a 50 mV s⁻¹.

Metal doped metal oxides or binary metal oxides have very efficient potential applications for the recent electrochemical sensors. Based on these materials can be ascribed to the higher electrochemical activity, enhanced electroactive surface property and excellent stability compare to the single metal oxides [68]. Especially, Ag@ZrO₂ displays improved resistance and greater electrochemical performance of TNZ, because of the good electron transfer movement and excellent synergistic effect between Ag and ZrO₂. Further, the electrode can absorb a more reactive substance of TNZ resulting in a rapid electroreduction process. As a consequence, we built a low-cost Ag@ZrO₂ modified electrode for TNZ determination.

Table 1. Comparison of TNZ at the various modified electrodes.

Modified electrodes	Methods	PB/pH	Detection potential (V)	WLR (μM)	LOD (μM)	Ref.
CPE ^a	DPV	3.0	-0.44	5–200	0.51	[11]
PANI ^b /GCE	SWV ^f	9.5	-0.65	10–60	4.71	[12]
poly(carmin)/GCE	DPV	5.7	-0.60	0.1–50	0.01	[13]
Au NPs-CNT ^c /GCE	LSV ^g	7.0	-0.55	0.1–50	0.01	[1]
1,4-BQM ^d /CPE	DPV	5.0	-0.39	1–300	0.11	[14]
Fe-MOF ^e /Pt/GCE	DPV	3.0	-0.38	0.02–525	0.043	[15]
Ag@ZrO ₂ /GCE	DPV	7.0	-0.29	0.2–414.5	0.073	This work

^aCarbon paste electrode. ^bPolyaniline. ^cCarbon nanotubes. ^d1,4-Benzoquinone. ^eMetal organic framework. ^fSquare wave voltammetry. ^gLinear sweep voltammetry.

3.8 Interference studies on TNZ

The interference studies of the proposed sensor were observed by the DPV analysis using 0.05 M PB (pH 7.0) in the presence of TNZ. Fig. 7c shows 10 μM of TNZ and metronidazole (MTZ-15 and 30 μM), the obtained current response of Ag@ZrO₂/GCE has no significant variation in the *I*_{pc} current and *E*_{pc} potential of TNZ and MTZ with a crucial potential difference were obtained at -0.29 and -0.33 V, respectively. Fig. 7d displays the DPV responses of individual and simultaneous detection of 10 μM TNZ and 75 μM MTZ wherein the signal of TNZ is slightly altered with the amount of 50 μM MTZ. The integrated peak currents of TNZ with MTZ show less than 5% interference-effect. Besides, 25 μM concentration of organic compounds namely 4-nitrophenol (4-NP), nitrofurantoin (NFT), furazolidone (FZ), glucose (Glu), uric acid (UA), and 50 μM of metal ions including Cd²⁺, Pb²⁺, and Na⁺ have selected interferents as 5 μM of TNZ are illustrated in Fig. 7e. The *I*_{pc} current of TNZ was not affected but signals lost only <7%. These experimental results confirm that the as-synthesized material showed good selectivity in potential interferents for the TNZ detection. The bar graph (Fig. 7f) of relative error (%) demonstrates the significant reduction current response of TNZ with variable interferents.

3.9 Stability (cyclic and storage), and precision study of the electrocatalyst

The CV of the Ag@ZrO₂/GCE electrode was developed for stability test (see Fig. 8a) over 75 cycles in 25 μ M TNZ containing PB (0.05 M, pH 7.0) at 50 mV s⁻¹. The Ag@ZrO₂ electrode shows only a 0.36 μ A decrease in the reduction current from the initial cycle (1st cycle) to the final cycle (75th cycle), demonstrating good stability in the optimized peak potential of -0.29 V, respectively. The storage stability was checked in 10 days at the Ag@ZrO₂ electrode in nitrogen saturated 0.05 M phosphate buffer as shown in Fig. 8b.

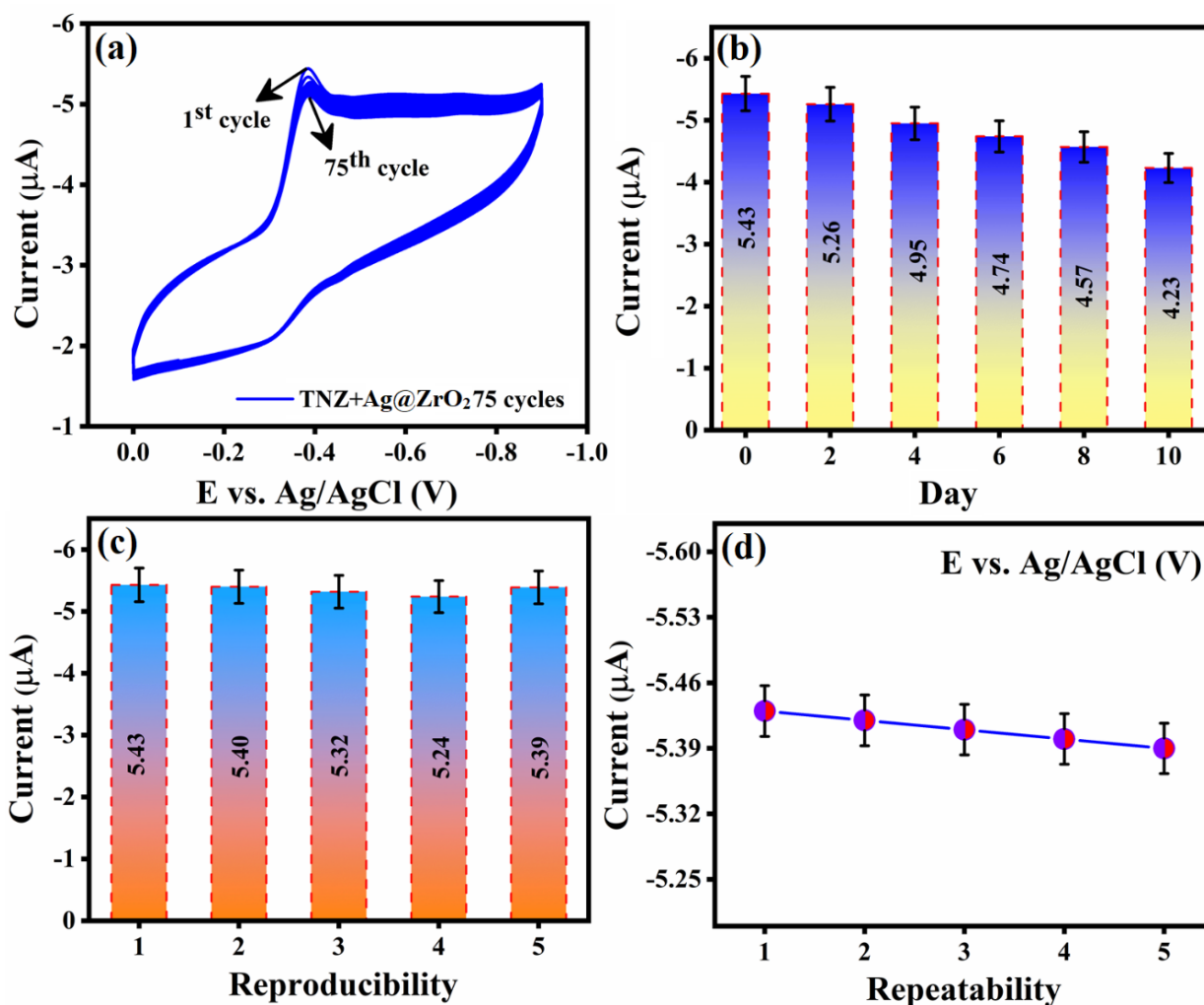


Figure 8. (a) The stability (over 75 cycles) of the proposed sensor with the addition of TNZ (25 μ M), (b) the storage stability of Ag@ZrO₂ modified electrode towards sensing of 25 μ M TNZ over 10 days, (c) CVs for reproducibility (five independent electrodes) and (d) repeatability (five successive electrodes) tests were carried out 25 μ M of TNZ with using pH 7.0 (0.05 M PB) at the scan rate of 50 mV s⁻¹.

This CV response was performed in 25 μ M TNZ every two days with obtained reduction peak current decreased only <14% after 10 days, which reveals the modified electrode has appreciable storage efficiency. Fig. 8c exhibits the reproducibility of five modified electrodes was estimated by CV in the

addition of 25 μM TNZ with the scan rate of 50 mV s^{-1} containing pH 7.0 (0.05 M PB). The observed RSD value is 2.65%, indicating the fabricated sensor is highly reproducible. We also studied the repeatability of the sensor by repeatedly using the modified Ag@ZrO_2 electrode with the measurements of 5 times in CV analysis for the spiked amount of 25 μM TNZ is presented in Fig. 8d. The 5 measurements of CV curves show a slight difference in peak current with the RSD of 3.30%, presenting well repeatable to the detection of TNZ. Furthermore, the morphology of five modified electrodes was studied by FESEM and XRD (before and after TNZ sensing) analysis as displayed in Fig. 9. The results indicated that the modified electrode was highly stable after the CV test in the presence of 50 μM TNZ.

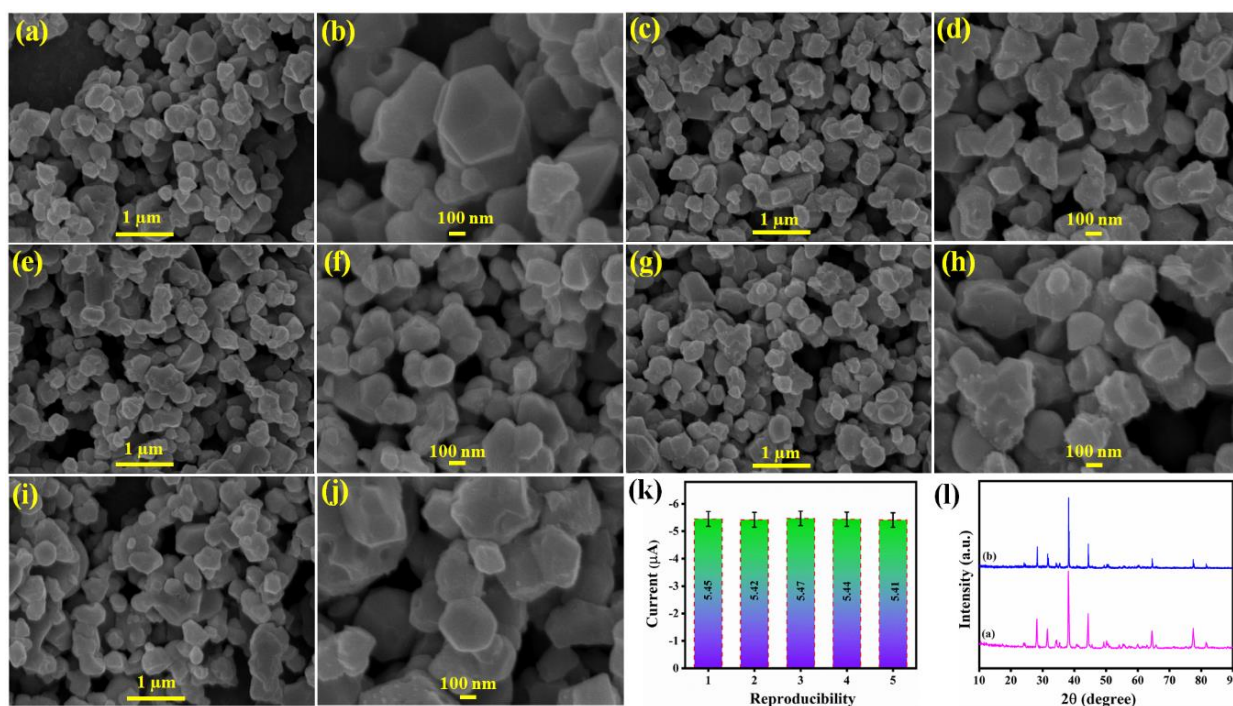


Figure 9. (a–j) Reproducibility test of five independent modified electrodes and (k) their CV response of 50 μM TNZ detection, and (l) XRD analysis for before (a) and after (b) addition of TNZ (50 μM) in nitrogen saturated 0.05 M PB (pH 7.0) at 50 mV s^{-1} .

3.10 Real sample test of TNZ

To study the practical application of the Ag@ZrO_2 modified electrode with various addition of TNZ from 0.50 μM to 4.25 μM in the human serum sample by using the DPV technique. The human serum was collected by a volunteer healthy people. The prepared serum sample was directly spiked into 0.05 M PB in pH 7.0 and results are observed based on the standard addition method in Fig. 10. The recoveries of the serum sample were succeeded to be 94.0% to 99.42% with an RSD of 2.24% for the detection of TNZ (Table 2). Hence, our fabricated $\text{Ag@ZrO}_2/\text{GCE}$ exhibits the excellent electrocatalytic performance of TNZ detection with good recoveries in the real human sample.

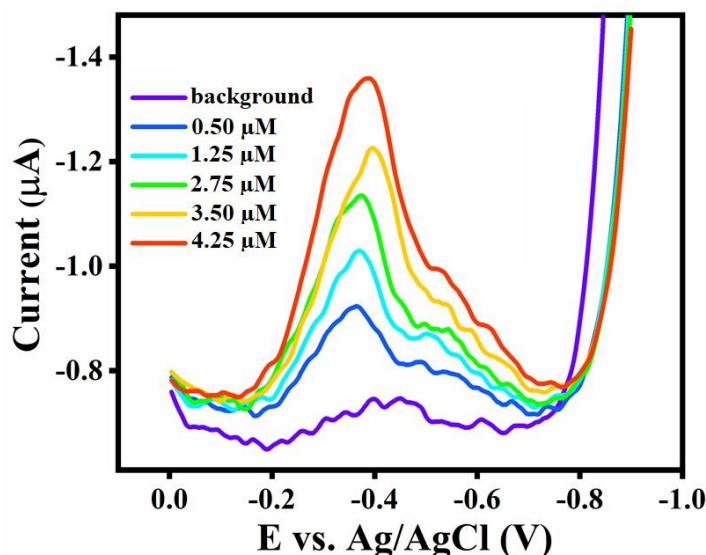


Figure 10. DPV response on Ag@ZrO₂ sensor for the human serum analysis with various concentrations of TNZ in the pH 7.0 (0.05 M PB solution).

Table 2. Real-time sensing of TNZ at the Ag@ZrO₂/GCE using human serum sample.

Sample	Spiked (µM)	Found (µM)	RSD (%)	Recovery (%)
Human serum	0.50	0.47	3.43	94.0
	1.25	1.23	2.71	98.40
	2.75	2.72	2.06	98.90
	3.50	3.48	1.64	99.42
	4.25	4.21	1.39	99.05

4. CONCLUSION

In summary, we developed low-cost Ag@ZrO₂ nanoparticles through the co-precipitation method. The as-prepared material was characterized by suitable spectroscopic measurements such as XRD, FT-IR, UV-DRS, PL, Raman, FESEM, EDX, and XPS analyzes. As a result, the Ag was successfully doped into ZrO₂ shows pebble-shaped stone-like nanoparticles morphology. The Ag@ZrO₂ shows superior reduction activity with a lower detection potential of -0.29 V towards TNZ than previously constructed electrodes at the first time. The Ag@ZrO₂ modified GCE displays extensive linearity of 0.2–414.5 µM, low detection limit with a sensitivity of 0.073 µM and 0.669 µA µM⁻¹ cm⁻² between reduction peak current and concentration of TNZ. The Ag@ZrO₂ sensor further established good selectivity in the sensing of TNZ with potential interferences were MTZ, 4-NP, NFT, FZ, Glu, UA, and metal ions as Cd²⁺, Pb²⁺, and Na⁺. The fabricated sensor demonstrates high stability, long-term efficiency, accuracy, and applicability of TNZ in human serum with results showing satisfactory. The overall performance suggests that the Ag@ZrO₂ nanoparticles can be used as a potential candidate for electrochemical sensors applications.

DECLARATION OF COMPETING INTEREST

The authors declare that they have no known competing financial interests or personal relationships that could have appeared to influence the work reported in this paper.

ACKNOWLEDGEMENT

The authors gratefully acknowledge the financial support of the National Taipei University of Technology and New Taipei Municipal TuCheng Hospital (Built and Operated by Chang Gung Medical Foundation) Joint Research Program, NTUT-NTMTCH-111-03 and CORPVVM0031. Financial supports of this work also by the Ministry of Science and Technology, Taiwan (MOST 110-2113-M-027-003 to SMC) is gratefully acknowledged.

References

1. S. Shahrokhian, S. Rastgar, *Electrochim. Acta*, 78 (2012) 422–429.
2. H.B. Fung, T.-L. Doan, *Clin. Ther.*, 27 (2005) 1859–1884.
3. A.K. De, A.K. Bera, B. Pal, *Int. J. Pharm. Sci. Res.*, 6 (2015) 3594.
4. B.A. Wood, J.K. Faulkner, A.M. Monro, *J. Antimicrob. Chemother.*, 10 (1982) 43–57.
5. G.P. Kumar, T.C. Sekhar, R.G.S. Madhuri, B.S. Murty, *Int. J. Appl.*, 3 (2011) 173–178.
6. M.M. Baraka, M.E. El-Sadek, L.M. Abdelaziz, S.S. Elbermawi, *Methods*, 28 (2014) 29.
7. R.I. El-Bagary, A.A. El-Zaher, E.F. Elkady, A.A. Mandour, *Futur. J. Pharm. Sci.*, 4 (2018) 185–190.
8. K.M. Elokely, M.A. Eldawy, M.A. Elkersh, T.F. El-Moselhy, *Int. J. Anal. Chem.*, 2011 (2011) 840178.
9. M. Bakshi, S. Singh, *J. Pharm. Biomed. Anal.*, 34 (2004) 11–18.
10. K. Basavaiah, P. Nagegowda, U. Chandrashekar, *Indian J. Chem. Technol.*, 12 (2005) 273–280.
11. A. Taye, M. Amare, *Bull. Chem. Soc. Ethiop.*, 30 (2016) 1–12.
12. R. Jain, P. Karolia, A. Sinha, *Adv. Polym. Technol.*, 37 (2018) 547–553.
13. C. Wang, F. Wang, C. Li, X. Xu, T. Li, C. Wang, *J. Pharm. Biomed. Anal.*, 41 (2006) 1396–1400.
14. Y. Nikodimos, B. Hagos, *J. Anal. Methods Chem.*, 2017 (2017) 1–10.
15. E. Saeb, K. Asadpour-Zeynali, *Microchem. J.*, 172 (2022) 106976.
16. G. Maduraiveeran, W. Jin, *Trends Environ. Anal. Chem.*, 13 (2017) 10–23.
17. H. Huang, L. Chen, S. Wang, P. Kang, X. Chen, Z. Guo, X.-J. Huang, *TrAC Trends Anal. Chem.*, 119 (2019) 115636.
18. J.M. George, A. Antony, B. Mathew, *Microchim. Acta*, 185 (2018) 1–26.
19. O.M. Ama, S.S. Ray, *Nanostructured Metal-Oxide Electrode Materials for Water Purification: Fabrication, Electrochemistry and Applications*, Springer Nature, (2020).
20. I.-J. Shon, *Int. J. Refract. Met. Hard Mater.*, 72 (2018) 257–262.
21. S. Furukawa, T. Masui, N. Imanaka, *J. Alloys Compd.*, 451 (2008) 640–643.
22. M.M. Mikhailov, V.A. Vlasov, S.A. Yuryev, V. V Neshchimenko, V. V Shcherbina, *Dye. Pigment.*, 123 (2015) 72–77.
23. A. Behbahani, S. Rowshanzamir, A. Esmaeilifar, *Procedia Eng.*, 42 (2012) 908–917.
24. G. Xu, Y. Zhang, C. Liao, C. Yan, *J. Am. Ceram. Soc.*, 87 (2004) 2275–2281.
25. M. Maham, M. Nasrollahzadeh, S.M. Sajadi, *Compos. Part B Eng.*, 185 (2020) 107783.
26. A. Husain, S. Ahmad, F. Mohammad, *Mater. Today Commun.*, 20 (2019) 100574.
27. L. Zhang, Q. Wang, Y. Qi, L. Li, S. Wang, X. Wang, *Sensors Actuators B Chem.*, 288 (2019) 347–355.
28. S. Zhou, M. Hu, X. Huang, N. Zhou, Z. Zhang, M. Wang, Y. Liu, L. He, *Microchim. Acta*, 187

- (2020) 1–9.
29. S.A. Shahamirifard, M. Ghaedi, Z. Razmi, S. Hajati, *Biosens. Bioelectron.*, 114 (2018) 30–36.
 30. N. Gao, C. He, M. Ma, Z. Cai, Y. Zhou, G. Chang, X. Wang, Y. He, *Anal. Chim. Acta*, 1072 (2019) 25–34.
 31. H. Mahajan, S.K. Arumugasamy, A. Panda, V. Sada, M. Yoon, K. Yun, *ACS Omega*, 5 (2020) 24799–24810.
 32. S.A. Alkahtani, A.M. Mahmoud, M.H. Mahnashi, R. Ali, M.M. El-Wekil, *Biosens. Bioelectron.*, 150 (2020) 111849.
 33. S. Vijayalakshmi, E. Kumar, P.S. Venkatesh, A. Raja, *Ionics (Kiel)*, 26 (2020) 1507–1513.
 34. T. Alizadeh, S. Nayeri, *J. Solid State Electrochem.*, 22 (2018) 2039–2048.
 35. P. Bansal, G. Bhanjana, N. Prabhakar, J.S. Dhau, G.R. Chaudhary, *J. Mol. Liq.*, 248 (2017) 651–657.
 36. X. Yin, X. Xie, L. Song, J. Zhai, P. Du, J. Xiong, *Appl. Surf. Sci.*, 440 (2018) 992–1000.
 37. T. Tao, Y. Zhou, C. He, H. He, M. Ma, Z. Cai, N. Gao, K. Wang, R. Zhu, G. Chang, *Electrochim. Acta*, 357 (2020) 136836.
 38. L. Li, Z. Wang, T. Wang, J. Gong, B. Qi, *J. Electroanal. Chem.*, 846 (2019) 113171.
 39. F. Gonella, G. Mattei, P. Mazzoldi, G. Battaglin, A. QuarantaG, *Chem. Mater.*, 11 (1999) 814–821.
 40. E.N.L. Rodrigues, E.J.P. Miranda Jr, M.M. Oliveira, *Mater. Sci. Forum*, 798 (2014) 69–74.
 41. E. Bharathi, G. Sivakumari, B. Karthikeyan, S. Senthilvelan, *Appl. Nanosci.*, 10 (2020) 3491–3502.
 42. T.M.S. Dawoud, V. Pavitra, P. Ahmad, A. Syed, G. Nagaraju, *J. King Saud Univ.*, 32 (2020) 1872–1878.
 43. V. Vinothkumar, M. Abinaya, S.-M. Chen, V. Sethupathi, V. Muthuraj, *Phys. E Low-Dimensional Syst. Nanostructures*, 134 (2021) 114865.
 44. P. Kaminski, *ChemEngineering*, 1 (2017) 18.
 45. M. Kohantorabi, M.R. Gholami, *New J. Chem.*, 41 (2017) 10948–10958.
 46. L. Chen, X. Zhao, B. Pan, W. Zhang, M. Hua, L. Lv, W. Zhang, *J. Hazard. Mater.*, 284 (2015) 35–42.
 47. A. Ananth, Y.S. Mok, *Nanomaterials*, 6 (2016) 42.
 48. M. Kumaresan, K.V. Anand, K. Govindaraju, S. Tamilselvan, V.G. Kumar, *Microb. Pathog.*, 124 (2018) 311–315.
 49. E. De la Rosa-Cruz, L.A. Diaz-Torres, P. Salas, V.M. Castano, J.M. Hernandez, *J. Phys. D. Appl. Phys.*, 34 (2001) L83.
 50. H.A.H. Alshamsi, B.S. Hussein, *Orient. J. Chem.*, 34 (2018) 1898.
 51. D. Eder, R. Kramer, *Phys. Chem. Chem. Phys.*, 4 (2002) 795–801.
 52. R.H. Dauskardt, D.K. Veirs, R.O. Ritchie, *J. Am. Ceram. Soc.*, 72 (1989) 1124–1130.
 53. S.L. Jangra, K. Stalin, N. Dilbaghi, S. Kumar, J. Tawale, S.P. Singh, R. Pasricha, *J. Nanosci. Nanotechnol.*, 12 (2012) 7105–7112.
 54. K. Karthik, M.M. Naik, M. Shashank, M. Vinuth, V. Revathi, *J. Clust. Sci.*, 30 (2019) 311–318.
 55. S.N. Basahel, T.T. Ali, M. Mokhtar, K. Narasimharao, *Nanoscale Res. Lett.*, 10 (2015) 73.
 56. D. Tan, G. Lin, Y. Liu, Y. Teng, Y. Zhuang, B. Zhu, Q. Zhao, J. Qiu, *J. Nanoparticle Res.*, 13 (2011) 1183–1190.
 57. P.K. Parashar, V.K. Komarala, *Sci. Rep.*, 7 (2017) 1–9.
 58. Y. Mi, J. Wang, Z. Yang, Z. Wang, H. Wang, S. Yang, *RSC Adv.*, 4 (2014) 6060–6067.
 59. S. Cui, L. Li, Y. Ding, J. Zhang, H. Yang, Y. Wang, *Talanta*, 164 (2017) 291–299.
 60. J.N. Appaturi, T. Pulingam, S. Muniandy, I.J. Dinshaw, L.B. Fen, M.R. Johan, *Mater. Chem. Phys.*, 232 (2019) 493–505.
 61. V. Vinothkumar, A. Sangili, S.-M. Chen, M. Abinaya, *Colloids Surfaces A Physicochem. Eng. Asp.*, 624 (2021) 126849.

62. T. Kokulnathan, S.-M. Chen, *ACS Appl. Mater. Interfaces*, 11 (2019) 7893–7905.
63. G. Kesavan, V. Vinothkumar, S.-M. Chen, *J. Alloys Compd.*, 867 (2021) 159019.
64. Y. Nikodimos, M. Amare, *J. Anal. Methods Chem.*, 2016 (2016) 1–7.
65. F. Ahmadi, J.B. Raof, R. Ojani, M. Baghayeri, M.M. Lakouraj, H. Tashakkorian, *Chinese J. Catal.*, 36 (2015) 439–445.
66. W. Geremedhin, M. Amare, S. Admassie, *Electrochim. Acta*, 87 (2013) 749–755.
67. V. Vinothkumar, M. Abinaya, S.-M. Chen, *J. Solid State Chem.*, 302 (2021) 122392.
68. P.S. Adarakatti, V. Udayakumar, *Ionics (Kiel)*, 27 (2021) 5309–5322.

© 2022 The Authors. Published by ESG (www.electrochemsci.org). This article is an open access article distributed under the terms and conditions of the Creative Commons Attribution license (<http://creativecommons.org/licenses/by/4.0/>).